Optik 125 (2014) 6898–6902

Contents lists available at ScienceDirect

Optik

journal homepage: www.elsevier.de/ijleo

Research on classification of LiDAR images derived from waveform decomposition over a suburban area

Wang Li[a,b], Zheng Niu[a,*], Bo Yu[a,b], Shuai Gao[a]

[a] The State Key Laboratory of Remote Sensing Science, Institute of Remote Sensing and Digital Earth, Chinese Academy of Sciences, Beijing 100101, China
[b] University of Chinese Academy of Sciences, Beijing 100049, China

ARTICLE INFO

Article history:
Received 30 November 2013
Accepted 8 June 2014

Keywords:
Image classification
LiDAR
Waveform decomposition

ABSTRACT

Light detection and ranging (LiDAR), as an active remote sensing technology, is characterized by providing high-precision geographical location information. In this study, we further explored its capability in image classification over a suburban area. Firstly, full waveforms of small footprint airborne LiDAR were decomposed into discrete point clouds. During the decomposition, six parameters describing the physical interaction between laser pulse and the targets were calculated. They are amplitude, pulse width, central position, range, backscatter cross-section and backscatter coefficient. Secondly, the point clouds were interpolated into raster. Correspondingly, six high spatial resolution images (0.5 m) were produced. Three classification models namely decision tree (DT), maximum likelihood (ML) and support vector machine (SVM) were established based on these images. The objects of interest were classified into buildings, trees, bare soil and crop land. Results showed that all these three models yielded high overall accuracy and kappa coefficient. SVM performed the best with the highest overall accuracy (87.85%) and kappa coefficient (83.29%). Therefore, we came to conclude that classification models can also achieve satisfactory classification accuracy on LiDAR images as they did on common remote-sensed images. In addition, our study proved that physical information derived from waveform LiDAR showed good potential in classification.

1. Introduction

Over the past one decade, light detection and ranging (LiDAR) has been widely used to record unique data about the vertical structure information of vegetation, especially in forestry. Numerous published studies have been focused on using LiDAR metrics to predict forest attributes, such as tree height [1], crown size [2], leaf area index [3], as well as biomass [4], etc. LiDAR metrics are mostly calculated by the height distribution of LiDAR point clouds. The point clouds can be obtained either by discrete laser scanner directly or by waveform laser scanner indirectly. The way to produce point cloud from waveform LiDAR is waveform decomposition [5–7]. However, apart from height distribution, some information reflecting the physical interaction between the laser pulse and the targets can be derived during the decomposition [5]. Physical information can be good indicators of the geometry characteristics and backscattering capability of the targets. That makes it possible for classification. A large number of classification models have been proposed and tested on both active and passive remote-sensed images. However, their capabilities have not fully been tested on LiDAR-derived images. Therefore, in this study, we aim to study classification only based on LiDAR-derived images. Firstly, we introduced the basic theory of waveform decomposition and the definition of six physical parameters. Then, six physical parameters were calculated during waveform decomposition and were interpolated into raster. After that, three classical models namely decision tree (DT), maximum likelihood (ML) and support vector machine (SVM) were established and compared based on these images. To the best of our knowledge, the latter two models have not been used for classifying images derived from waveform decomposition.

2. Methodology

2.1. LiDAR data

In this study, small footprint waveform data were acquired by the Riegl LMSQ560 during the Watershed Allied Telemetry Experimental Research (WATER) [8] in 2008 over the Heihe River Basin in northwestern China. The study area in this study is part of Zhangye city including buildings, trees, bare land and crop land. The

* Corresponding author. Phone & fax: +010-648892150.
E-mail address: niuz@irsa.ac.cn (Z. Niu).

http://dx.doi.org/10.1016/j.ijleo.2014.06.172
0030-4026/

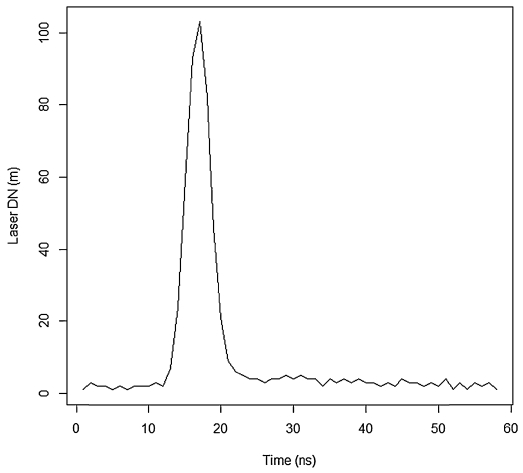

Fig. 1. The standard emitted waveform of Riegl LMSQ560.

sensor emits a Gaussian-shaped system waveform (Fig. 1) and records return waveform simultaneously at a flight height about 700 m above ground. The pulse width at half maximum of the emit pulse is 4 ns and vertical resolution is about 0.6 m.

2.2. Waveform decomposition

In theory, LiDAR waveform can be treated as a sum of several Gaussian functions [5,9]. Each Gaussian function can be described as following equations:

$$f(t_i) = h_i \exp\left[-\frac{(t_i-\alpha_i)^2}{{w_i}^2}\right], \tag{1}$$

$$f(t) = \sum_{i=1}^{n} f(t_i), \tag{2}$$

where $f(t_i)$ is a single Gaussian component, h_i is amplitude, α_i is central position, w_i is pulse width, n is the number of targets within the travel path of the laser pulse. $f(t)$ is the sum of n Gaussian components. In this study, we used a stepwise decomposition algorithm [7] to estimateh_i, α_i and w_i of each Gaussian function.

2.3. Calculation of range R backscatter cross-section σ, and backscatter coefficient γ

Backscatter cross-section is defined as the effective area of collision of the laser beam and the target with directionality and strength of reflection taken into account. It is defined as below:

$$\sigma_i = \frac{4\pi}{\Omega_i}\rho_i A_i, \tag{3}$$

where σ_i is the backscatter cross-section, Ω_i is the scattering solid angle of the target, ρ_i is the reflectivity of the target and A_i is the effective area of collision of target. For extended targets that are larger than the footprint size of the laser beam, the collision area is equal to the footprint area [6]. The foot print area A_{fi} can be calculated using the following equation:

$$A_{fi} = \frac{\pi {R_i}^2 {\beta_i}^2}{4}, \tag{4}$$

where R_i is the range between the laser sensor and the target, β_i is the beam width of laser pulse.

On the other hand, backscatter cross-section can be calculated using parameters obtained by the waveform decomposition [5]. It is defined as below:

$$\sigma_i = C_{const} {R_i}^4 h_i w_i, \tag{5}$$

where C_{const} is the calibration constant. Here, we chose the central position of a single peak in a waveform as an estimate of range. To calculate C_{const} we assumed that the asphalt road in the study area to be an ideal Lambertian scatterer and its reflectivity was 0.2. Therefore, C_{const} was calculated using the R, h and w of some return pulses of asphalt road. After that, all the backscatter cross-sections of the other targets during the waveform composition were calculated.

Since the illuminated footprint area of the laser pulse at different range is different, and the targets may be area extended, backscatter coefficient γ_i was proposed [10] to describe the cross-section per unit illuminated area. It can be described as below:

$$\gamma_i = \frac{\sigma_i}{A_i}. \tag{6}$$

Based on above methods, we finally calculated six physical parameters for each laser pulse. Each parameter can be interpolated into raster at a resolution of 0.5 m in ArcGIS9.3, which will be used in the later classification.

2.4. Classification models

Three classification models including decision tree (DT), maximum likelihood (ML) and support vector machine (SVM) were tested for their performance in classification. All these three models have been widely used in classification on common remote-sensed images. Decision tree, as a simple and fast approach, has been proved efficient in the classification of vegetation using the parameters derived from waveform decomposition [6]. However, to the best of our knowledge, the latter two models have not been used for classifying images derived from waveform decomposition.

Decision tree is actually a threshold-based classifier in the form of a tree structure. The tree structure includes decision node, leaf node and path. It classifies the targets starting from the root of the tree and moving through it until a leaf node. Generally, the more complicated the tree structure is, the less accurate the classification result will be. Selecting the most appropriate attribute to make a decision at each node is critical to the final result.

Maximum likelihood model is a widely used supervised classification method in remote sensing image analysis. It evaluates the probability that a given pixel belongs to a specific class. Discriminate functions for each pixel in the image are used to assess the probability. The functions are defined as below [11]:

$$g_i(x) = \ln p(\omega_i) - \frac{1}{2}\ln|\Sigma_i| - \frac{1}{2}(x-m_i)^t \sum_i^{-1}(x-m_i), \tag{7}$$

where i is class index, x is the pixel value, $p(\omega_i)$ is the probability that class ω_i occurs in the image and is assumed the same for all classes, m_i and Σ_i are the mean vector and covariance matrix of the data in classω_i. Each pixel will be assigned to the class that holds the highest probability.

Support vector machine is a non-parametric classification method that separates the pixels by a decision surface with the maximum margin among different classes [12]. It is actually an optimization problem with four basic kernels. Here, we used the radial basis function kernel. The kernel is defined as below:

$$K(x_i, x_j) = \exp(-\lambda||x_i - x_j||^2), \lambda > 0, \tag{8}$$

where λ is the gamma term in the kernel function, x_i and x_j are training vectors.

Referred to the airborne CCD image, we randomly selected two groups of area of interest (AOI) from the LiDAR images. One group

Table 1
Basic statistics of LiDAR-derived parameters for the area of interest.

Parameters	Basic statistic				Class and pixels
	Min	Max	Mean	Stdev	
Hm	0.00	1.96	0.58	0.37	Buildings (463, 235)
Wm	2.58	4.00	2.84	0.17	
b	15.25	18.56	16.89	0.66	
Range	699.84	706.69	703.37	2.03	
Deta	0.09	0.24	0.15	0.04	
Gama	0.87	2.48	1.50	0.41	
Hm	4.42	20.33	12.99	5.39	Trees (243, 137)
Wm	4.73	7.93	7.13	0.59	
b	11.71	47.00	18.30	2.98	
Range	686.05	701.61	693.64	4.82	
Deta	0.04	0.08	0.06	0.01	
Gama	0.39	0.84	0.61	0.08	
Hm	0.00	0.24	0.04	0.05	Baresoil (289, 154)
Wm	3.32	6.95	4.72	0.53	
b	14.95	19.28	17.05	0.68	
Range	706.75	708.26	707.49	0.37	
Deta	0.04	0.09	0.07	0.01	
Gama	0.42	0.92	0.71	0.07	
Hm	0.00	0.22	0.06	0.05	Crop (339, 116)
Wm	2.65	2.94	2.77	0.07	
b	15.71	17.90	16.62	0.50	
Range	707.77	708.85	708.26	0.33	
Deta	0.08	0.10	0.09	0.01	
Gama	0.77	1.02	0.91	0.06	

Note: h = amplitude; w = pulse width; α = central position; R = range; σ = backscatter cross-section; γ = backscatter coefficient; min = minimum value; max = maximum value; mean = average value; Stdev = standard deviation; numbers in parentheses stand for the number of pixels for training data and testing data, respectively.

was used to train the classification models; the other was used to test the results of the classification. Our objects of interest are buildings, trees, bare land and crop land. Basic statistics for the area of interest were calculated and shown in Table 1. Based on these statistics, a decision tree was established as shown in Fig. 2. Not all the parameters were used in the decision tree approach, because some cannot clearly distinguish the targets (e.g. α_i, σ) with one threshold only. However, all the parameters were used in the latter two models.

3. Results and discussion

3.1. Physical parameters derived from waveform decomposition

All the six physical parameters derived from waveform decomposition were interpolated into raster (0.5 m) as shown in Fig. 3. The amplitude values observed over the trees in the image are much higher than those of the crop land and bare soil, which

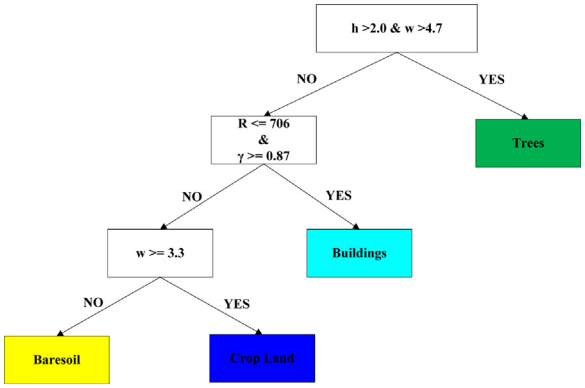

Fig. 2. Tree structure of decision tree model. h = amplitude; w = pulse width; R = range; γ = backscatter coefficient.

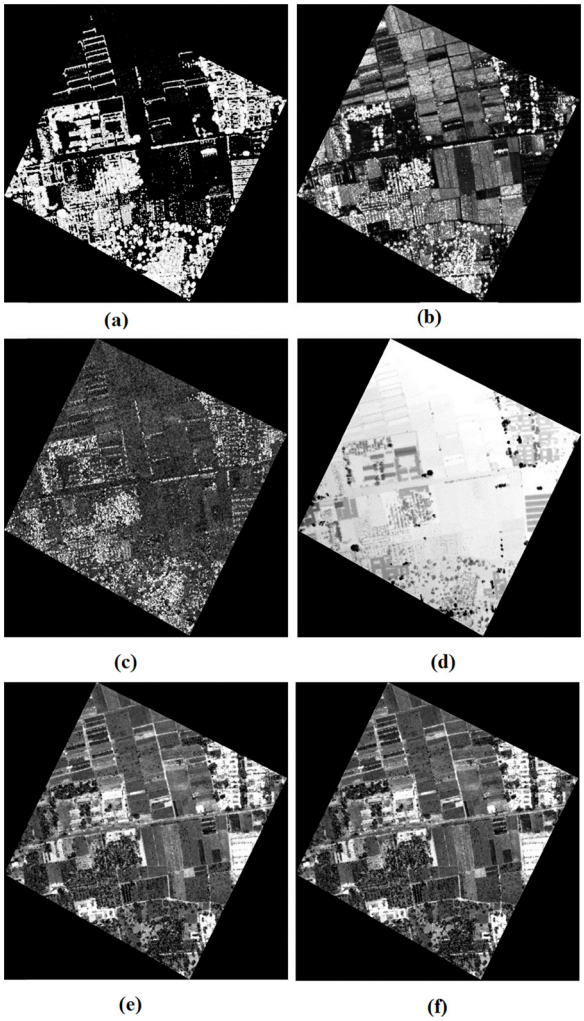

Fig. 3. Images of physical parameters obtained by waveform decomposition of small footprint airborne laser scanner (ALS): (a) the amplitude image; (b) the pulse width image; (c) the central position image; (d) the range image; (e) the backscatter cross-section image; (f) the backscatter coefficient image.

exhibits a high contrast. By contrast, the pulse width image can easily distinguish the vegetation (trees and crop land) from artificial classes (buildings and bare soil). Compared with vegetation, the pulse width of buildings and bare soil are fairly narrow. The central position image and range image show a comparatively low contrast. These two parameters are related to distance between the laser sensor and the targets. However, the range difference between the low classes and the high classes are still obvious as shown in Fig. 3(d). For instance, the pixel values of tall buildings and trees are much lower than those of ground classes. Backscatter cross-section (Fig. 3(e)) and backscatter coefficient (Fig. 3(f)) show a consistent pattern where the area-extended classes (e.g. buildings) obtained higher values. The distinctive contrasts between different classes are easily visible and might be helpful to the image classification.

3.2. Classification performance of three models

Confusion matrix was calculated to evaluate the result of classification. A visual result of the classification is shown in Fig. 4 and the accuracy evaluation is shown in Table 2. For all the classes, both producer's accuracy (Pro's a.) and user's accuracy (Usr's a.) are above 70% in the three models. Among all the classes, crop land which covered a large part of the study area showed a consistent high accuracy observed from its producer's accuracy (90.26–99.35%) and

Table 2
Confusion matrices and classification accuracies yielded by three models.

Method	Class	Ground truth (pixels)				Total	Usr's a. (%)
		Buildings	Trees	Bare soil	Crop		
Decision tree	Buildings	178	2	9	0	189	94.18
	Trees	0	102	0	6	108	94.44
	Bare soil	35	2	95	0	132	71.97
	Crop	22	25	12	154	213	72.30
	Total	235	131	116	160	642	
	Pro's a. (%)	75.74	77.86	81.90	96.25		
	O.A.a (%) = 82.40	Kappa coef (%) = 76.15					
Method	Class	Ground truth (pixels)	Total	Usr's a. (%)			
		Buildings	Trees	Bare soil	Crop		
Max likelihood	Buildings	200	7	16	0	223	89.69
	Trees	21	120	0	15	156	76.92
	Bare soil	14	0	87	0	101	86.14
	Crop	0	10	13	139	162	85.80
	Total	235	137	116	154	642	
	Pro's a. (%)	85.11	87.59	75.00	90.26		
	O.A.a (%) = 85.05	Kappa coef (%) = 79.59					
Method	Class	Ground truth (pixels)	Total	Usr's a. (%)			
		Buildings	Trees	Bare soil	Crop		
SVM	Buildings	209	2	34	0	245	85.31
	Trees	0	120	0	1	121	99.17
	Bare soil	24	4	82	0	110	74.55
	Crop	2	11	0	153	166	92.17
	Total	235	137	116	154	642	
	Pro's a. (%)	88.94	87.59	70.69	99.35		
	O.A.a (%) = 87.85	Kappa coef (%) = 83.29					

Note: Usr's a. = user's accuracy; Pro's a. = producer's accuracy; O.A.a = overall accuracy; Kappa coef = Kappa coefficient.

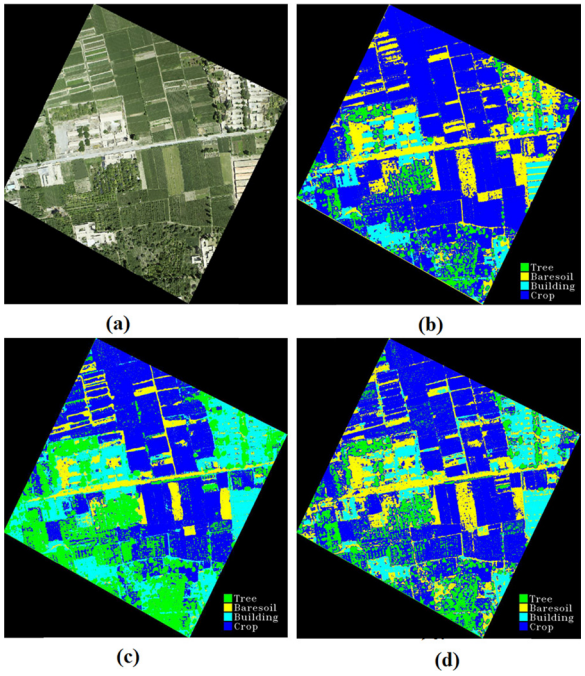

Fig. 4. The CCD images of the study area and the results of classification: (a) CCD image; (b) classification result of decision tree (DT) model; (c) classification result of maximum likelihood (ML) model; (d) classification result of support vector machine (SVM) model.

user's accuracy (72.3–92.17%). Bare soil showed a comparatively poor accuracy by being misclassified to buildings and crop land, which is obvious in the confusion matrices.

For the three models, both the overall accuracy (O.A.a) and kappa coefficient (Kappa coef) are high. SVM model yielded the highest accuracy (O.A.a = 87.35%, Kappa coef = 83.29%) among the three models. Three of the four classes except bare soil showed a consistently high accuracy in SVM model. For the classification result of DT model (Fig. 4(b)), buildings and crop land were clearly identified. The outlines of buildings in Fig. 4(b) are fairly clear, which shows a better visual result than the other two models. However, some trees were mistakenly classified as crop land by the DT model telling from its producer's accuracy as well as the classification map. In addition, some areas of buildings were classified as bare soil (upper right corner in Fig. 4(b)), which produced a comparatively low producer's accuracy of buildings. The comparatively low accuracy of DT model is directly related to the determination of the threshold used in each leaf node. ML model played a poor role in distinguishing trees from crop land as shown in the lower left corner in Fig. 4(c). This is likely due to the inaccuracy estimation of covariance matrix [13]. An improper ratio between the number of available training samples and features might be presented during the classification procedure.

4. Conclusion

This study extended previous studies on LiDAR technology which focused on using LiDAR metrics to obtain vegetation structure information. We explored to produce a series of images representing different physical information by waveform decomposition. Three classification models were tested and compared on these LiDAR images over a suburban area. Results showed that fairly high classification accuracy was yielded by the three classification models, especially SVM. This indicates that classical image-analysing methods have a large potential application for the analysis of waveform LiDAR-derived images. In addition, our study proved that physical information derived from waveform LiDAR showed good potential in classification. Still, higher classification accuracy might be obtained by fusing this physical information with other remote-sensed images.

Acknowledgements

This work was funded by China's Special Funds for Major State Basic Research Project (2013CB733405, 2010CB950603) and

project supported by the National Natural Science Foundation of China (41201345). We thank all the people working in the projects.

References

[1] C. Edson, M.G. Wing, Airborne light detection and ranging (LiDAR) for individual tree stem location, height, and biomass measurements, Remote Sens. 3 (2011) 2494–2528.
[2] B. Hu, J. Li, L. Jing, A. Judah, Improving the efficiency and accuracy of individual tree crown delineation from high-density LiDAR data, Int. J. Appl. Earth Obs. Geoinf.V 26 (2014) 145–155.
[3] D. Riaño, F. Valladares, S. Condés, E. Chuvieco, Estimation of leaf area index and covered ground from airborne laser scanner (LiDAR) in two contrasting forests, Agr. Forest Meteorol. 124 (2004) 269–275.
[4] S.C. Popescu, Estimating biomass of individual pine trees using airborne LiDAR, Biomass Bioenerg. 31 (2007) 646–655.
[5] W. Wagner, A. Ullrich, V. Ducic, T. Melzer, N. Studnicka, Gaussian decomposition and calibration of a novel small-footprint full-waveform digitising airborne laser scanner, Isprs J. Photogramm. 60 (2006) 100–112.
[6] W. Wagner, M. Hollaus, C. Briese, V. Ducic, 3D vegetation mapping using small-footprint full-waveform airborne laser scanners, Int. J. Remote Sens. 29 (2008) 1433–1452.
[7] Y. Qin, B. Li, Z. Niu, W. Huang, C. Wang, Stepwise decomposition and relative radiometric normalization for small footprint LiDAR waveform, China Ser. D. 54 (2010) 625–630.
[8] X. Li, X. Li, Z. Li, M. Ma, J. Wang, Q. Xiao, et al., Watershed allied telemetry experimental research, J. Geophys. Res. 114 (2009) D22103.
[9] Y. Qin, T.T. Vu, Y. Ban, Toward an optimal algorithm for LiDAR waveform decomposition, IEEE Geosci. Remote Sens. Lett. 9 (2012) 482–486.
[10] W. Wagner, Radiometric calibration of small-footprint full-waveform airborne laser scanner measurements: basic physical concepts, Isprs J. Photogramm. 65 (2010) 505–513.
[11] J.A. Richards, Xiuping Jia, Remote Sensing Digital Image Analysis, Springer-Verlag, Berlin, 1999, pp. 194–196.
[12] C.W. Hsu, C.C. Chang, C.J. Lin, A practical guide to support vector classification, J. Mach. Learn. Res. 5 (2007) 975–1005.
[13] F. Melgani, L. Bruzzone, Classification of hyperspectral remote sensing images with support vector machines, IEEE. Trans. Geosci. Remote Sens. 42 (2004) 1778–1790.